Deformation mechanisms at the tip of internal fatigue cracks in vacuum and in the presence of an air environment in a Ti alloy

Louis Hébrard, Thierry Palin-Luc, Nicolas Ranc, Arnaud Weck, Thierry Douillard, Nicholas Blanchard, Sylvain Dancette, Jean-Yves Buffiere

International Journal of Fatigue 193 (2025) 108729

Contents lists available at ScienceDirect

International Journal of Fatigue

journal homepage: www.elsevier.com/locate/ijfatigue

Deformation mechanisms at the tip of internal fatigue cracks in vacuum and in the presence of an air environment in a Ti alloy

Louis Hébrard [a], Thierry Palin-Luc [b,c], Nicolas Ranc [d], Arnaud Weck [e,f,g], Thierry Douillard [a], Nicholas Blanchard [h], Sylvain Dancette [a,i], Jean-Yves Buffiere [a,*]

[a] INSA Lyon, MATEIS, CNRS UMR 5510, F-69621 Villeurbanne, France
[b] Univ. Bordeaux, CNRS, Bordeaux INP, I2M, UMR 5295, F-33400, Talence, France
[c] Arts et Metiers Institute of Technology, CNRS, Bordeaux INP, Hesam Universite, I2M, UMR 5295, F-33400 Talence, France
[d] PIMM Laboratory, Arts et Metiers Institute of Technology, CNRS, Cnam, HESAM University, Paris, France
[e] Department of Mechanical Engineering, University of Ottawa, 150 Louis Pasteur, Ottawa, ON, K1N 6N5, Canada
[f] Centre for Research in Photonics, University of Ottawa, 25 Templeton, Ottawa, ON, K1N 6N5, Canada
[g] Department of Physics, University of Ottawa, 150 Louis-Pasteur, Ottawa, ON, K1N 6N5, Canada
[h] Universite Claude Bernard Lyon 1, CNRS, Institut Lumière Matière, UMR5306, F-69100, Villeurbanne, France
[i] ElyTMaX IRL3757, CNRS, Université de Lyon, INSA Lyon, Centrale Lyon, Université Claude Bernard Lyon 1, Tohoku University, Sendai 980-8577, Japan

ARTICLE INFO

Keywords:
Internal fatigue cracks
Ti-6Al-4V
Twining
Nanograin
Environment

ABSTRACT

Ultrasonic fully reversed tension fatigue tests have been performed in the Very High Cycle Fatigue (VHCF) regime ($N_R > 10^7 - 10^8$ *cycles*) on Ti-6Al4V specimens containing a controlled internal notch. Two sets of samples have been used. The first one contains a central chimney along the specimen longitudinal axis which brings air to the internal notch; in the second series the notches are not connected to the surface. The microstructure present below the fracture surface of the broken specimens has been studied by electron microscopy (EBSD, TKD and TEM). The formation of nanograins and nanovoids was observed below the surface of the cracks growing in a vacuum environment but not below the surface of cracks connected with ambient air. In the latter case extensive striations were observed. Below each striation the formation of tensile $\{10\bar{1}2\}$ twins was observed.

1. Introduction

During fatigue at very low stress levels (typically less than 25% of the yield stress with a number of fatigue cycles larger than 10^8 cycles) the failure of metallic specimens is generally due to the propagation of an internal crack. In this case, a circular region, called Fish-Eye (FE), can be observed on the fracture surface around the initiation site. A so-called Rough Area (RA) is observed within the FE region; the name of this region varies according to authors and to the type of material studied as explained in [1].

In the Ti-6Al-4V alloy studied here, SEM observations within the RA show some facets scattered within large zones with a granular aspect [2–4]. The normals of the facets appear roughly aligned with the $\vec{c}$ -axis of the Hexagonal Close Packed (HCP) structure of the α phase, which is predominant in Ti-6Al-4V . For example, Pilchak et al. [5] have shown, using EBSD measurements, that the angle between the facet normals and the $\vec{c}$ -axis is comprised between −20° and 40°. The texture of the material seems to have an influence on the plane of the facets: in Ti-6Al-4V wires with a strong prismatic texture,[1] Evenaerts et al. [6] have observed in the RA an important majority of facets not parallel to the basal plane but to the prismatic planes of the HCP structure.

The formation of the granular region between the facets seems strongly correlated to the presence of vacuum at the crack tip (which is assumed in the presence of an internal crack): Oguma et al. [4] have shown in Compact Tension (CT) specimens that the granular regions observed for long cracks grown in vacuum disappear in the presence of air, quasi cleavage facets replacing the granular area. Similar observations have been made by Yoshinaka et al. [7] in the case of small (below 1 mm) surface cracks: when a 10^{-6} Pa pressure (High Vacuum condition) is applied around the specimens a "granular and rounded" aspect is observed close to the initiation site on the crack surface. In presence of atmosphere, the authors observe an "angular and sharp" zone close to the initiation site surrounded by a "larger flat striated zone".

* Corresponding author.
E-mail address: jean-yves.buffiere@insa-lyon.fr (J.-Y. Buffiere).

[1] (*i.e.* The majority of grains with their prismatic $\{10\bar{1}0\}$ planes aligned with the loading direction)

https://doi.org/10.1016/j.ijfatigue.2024.108729
Received 26 August 2024; Received in revised form 16 October 2024; Accepted 21 November 2024
Available online 3 December 2024

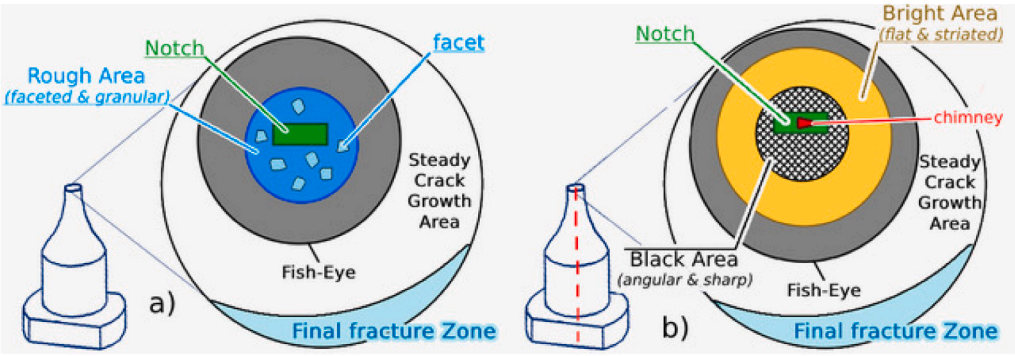

Fig. 1. Graphical summary of the fractographic features observed in Ti-6Al-4V specimens with internal defects. (a) sample without chimney: a fine granular region containing crystallographic facets around the notch (b) sample with chimney: a faceted region (which appears dark in the optical microscope) is observed close to the notch; it is surrounded by a relatively flat region (which appears bright in the optical microscope) containing extensive striations (adapted from [16]). The location of the chimney (with a triangular cross section) within the sample is indicated by the red dot line/triangle.

Within the granular regions of the RA, underneath the fracture surface, the presence of small grains has been reported several times in steels [8–10] and also in Ti alloys first by Heinz [11], then, in more detailed studies, by Su et al. [12] and Chang et al. [13] using TEM observations.

Several mechanisms have been suggested to explain the presence of the small/nano grains. In steels, the presence of inclusions (carbides) or of hydrogen contained in the inclusions is thought to be responsible for the formation of the small grains by different researchers [14,15]. For Ti alloys and also for steels a so-called Numerous Cyclic Pressing (NCP) model has been proposed by Hong's group [1]. It states that the repeated pressing between the crack surfaces during fatigue cycling can lead to the formation of a nanograin layer immediately below the crack lips. Also for Ti alloys, and because the Fine Grain Area is only observed for specimens cycled in vacuum and not in air, Oguma & Nakamura [4] have suggested a mechanism of cold-welding occurring between the two lips of an internal crack.

In a previous paper [16] Synchrotron X-ray tomography was used to characterize the propagation of small (below 1 mm in diameter) internal fatigue cracks initiated from artificial defects in Ti-6Al-4V specimens during ultrasonic fatigue tests leading to very long fatigue lives. Due to the presence of a chimney (with a cross section of about 20 μm × 250 μm) connecting the internal artificial defect to the laboratory air (see Fig. 1b), the internal cracks were growing either in vacuum or in air leading to very different growth rates and fracture surfaces. For the internal cracks growing in vacuum (and with a slow growth rate) the typical facets scattered within the granular regions were observed while for the cracks growing with some connection with air (large crack growth rates), a highly faceted region surrounded by quasi cleavage facets showing extensive striations was observed close to the defect (see Fig. 1).

The present paper complements this initial work [16] and goes deeper into the analysis of the deformation mechanisms at the crack tip by characterizing the microstructure of the material immediately beneath the fracture surface in the regions corresponding to the first stages of growth in presence of vacuum or of air. By analyzing transverse sections taken perpendicular to the average crack plane it was found that the environment has a major influence on the crack tip deformation processes occurring during the propagation of the internal cracks.

2. Material and experimental method

The material, specimens, fatigue machine and test protocol have been described in detail in [16,17]. In the following text, only the most relevant points are highlighted.

Table 1
Chemical composition of the studied Ti-6Al-4V (mass %).

Al	V	Fe	O	C	N	H	Y	Ti
6.43	4.10	0.15	0.18	0.01	0.004	0.004	<0.001	Bal.

2.1. Material

The studied material is a Ti-6Al-4V alloy bought from the Timet company in the form of a 15 mm thick plate. Its chemical composition is given in Table 1. After hot rolling at 750 °C an equiaxed microstructure is observed at the center of the plate (where the specimens are extracted) with small Body Centered Cubic (BCC) β regions located at the boundaries of large Hexagonal Close Packed (HCP) α regions (surface fraction ~ 94 %). The average α grain size determined from area fraction measurement in Electron Backscatter Diffraction (EBSD) maps is 10 ± 1 μm.

EBSD analysis of the microstructure in the gauge length of the fatigue specimens has revealed the presence of macrozones which can be visualized in Fig. 2. Within those zones, a large number of grains have their $\vec{c}$ -axis parallel to the rolling direction (Z direction in the figure) or to the Rolling Transverse direction (Y direction in the figure). This is a classical microstructure inherited from the hot rolling process in this type of material [18].

2.2. Fatigue specimens and ultrasonic tests

The tested fatigue specimens contained artificial internal defects (notches); they were produced by SPS diffusion bonding of two plates as explained in [19,20]. For some specimens, a narrow chimney parallel to the specimen axis (chimney) linked the notch to the surface of the specimen and allowed ambient air to reach the internal defect and, after crack initiation, the crack tip via the notch.

X-ray tomography is, for the moment, the only technique which can provide *direct* images of cracks growing in the bulk of metallic materials during in situ loading (see for example [21] for a review). In Ti-6Al-4V, synchrotron tomography has been used during in situ interrupted fatigue tests for studying the propagation of natural internal fatigue cracks [22,23] in the high cycle fatigue region of the S-N curve ($N_R < 10^7$ cycles). For the work presented here, a dedicated ultrasonic fatigue testing machine was used to enable X-ray tomography during in situ tests at a synchrotron facility [24]. The specimens have been cycled at 20 kHz with a loading ratio R = −1. The loading direction is parallel to the rolling direction and perpendicular to the average notch plane. During the tomographic scans the specimens were kept

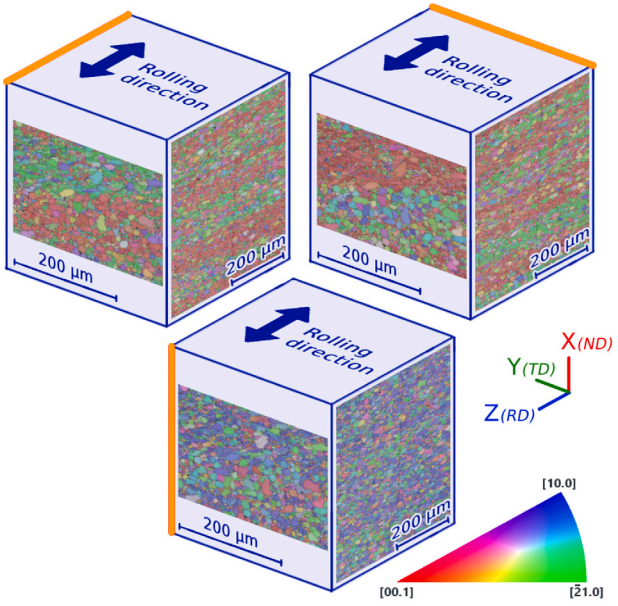

Fig. 2. Microstructure of the rolled sheet used in this study. The crystallographic orientations are displayed on the faces of each cube following the color code of the Inverse Pole Figure (IPF) and according to the orange lines direction on the cube edges. The rolling process has created macrozones containing grains with their $\vec{c}$ -axis in the Y and Z directions. A 5°misorientation is used.

under static load (80% of the stress amplitude) to hold the cracks open and enhance their visibility in the reconstructed images. Depending on the synchrotron beamline used, the scan duration varied between 5 to 10 min. Following the tests, the 3D crack shapes were extracted from the reconstructed tomographic images, enabling the measurement of growth rates along the crack front within the FE region.

For Paris curves, the effective SIF range ΔK_{eff} is used. it is approximated as $\Delta K_{eff} = K_{max} - K_{op}$ with $K_{op} = 0$ MPa.$\sqrt{\text{m}}$ (the opening load at 20 kHz cannot be measured). That means that no propagation has been assumed during the compressive part of the cycle, no closure effect in the tensile part and $\sigma_{max} = \Delta\sigma/2$ because of the fully reversed loading.[2] Details on the crack thresholding procedure and on the $da/dN = f(\Delta K_{eff})$ curves calculation can be found in [16].

2.3. Post mortem analysis of the microstructure below the fracture surfaces

The fracture surfaces of the specimens with or without chimney have been studied using scanning (SEM) and transmission (TEM) electron microscopy. The first of those two techniques has been used (i) directly on the fracture surfaces to try to obtain the crystallographic orientation of the facets observed within the RA [16] and (ii) on polished sections perpendicular to the (average) crack plane and containing the specimen longitudinal axis (loading direction). Two methods were used to produce those sections: argon broad ion beam (BIB) milling using an Ilion II cross polisher and Focused Ion Beam (FIB) machining in a SEM. The first method provides a relatively "large" region (~ 1 mm long and 150 µm wide) containing between ten to twenty grains for EBSD analysis. FIB machining produced an area with a smaller size (20 µm deep) compensated by its small thickness (~ 150 nm) which allows high resolution orientation analysis in transmission mode either in SEM (Transmission Kikuchi Diffraction technique, TKD) or in TEM (JEOL JEM-2100 LaB_6).

[2] σ is the value of the longitudinal stress (averaged in the section) along the sample axis in the absence of defect.

Although EBSD has modernized materials characterization by providing local orientation and texture information, its spatial resolution is limited by the size of the Back Scattered Electron (BSE) emission volume (which depends on the accelerating voltage, the atomic number of the target and its density). The lateral spatial resolution of the EBSD technique is generally limited to around 50 nm [25]. The characterization of nanocrystalline structures by EBSD is therefore compromised, except for a few heavy elements. To improve the spatial resolution of EBSD, another approach is to thin the specimen to a thickness less than the maximum depth of BSE emission. Building on this original idea, the past decade has seen the emergence of the TKD technique, which offers a spatial resolution below 10 nm [26–28]. TKD is typically performed at an accelerating voltage of around 30 kV. Under these conditions, the transmitted diffracted signal mostly originates from the bottom layers of the foil as demonstrated by Keller et al. [26]. Therefore, the lateral spatial resolution of the TKD technique is not as fine as that of techniques using Nano Beam Diffraction in TEMs [29]. Since the emergence of the TKD technique, many applications have been reported with an increasing interest and impact on the understanding of materials science issues. Orientation mapping is currently the most reported TKD application in the literature. The main purpose is the characterization of grains and nano-grain structures [30] and deformation in metals and alloys [31–34]. In this work, EBSD and TKD data were collected with a conventional off-axis detector geometry using an Oxford Symmetry EBSD camera (with a CMOS-based commercial EBSD detector, Oxford Instruments, High Wycombe, UK) on a Zeiss Supra 55 VP (Zeiss, Oberkochen, Germany) operated at 30 kV.

3. Results

3.1. Fatigue specimens without chimney

All the specimens containing an internal notch not connected with ambient air failed from a crack initiated at the notch and with fatigue lives shorter than those of un-notched specimen at the same stress level as shown in Fig. 3. The $da/dN = f(\Delta K_{eff})$ curves are in very good agreement with those obtained by Geathers et al. [35] on the same material as shown in Fig. 4. Close to the notch, the fracture surface exhibited the typical granular region containing some facets with a crystallographic aspect (see Fig. 5). Two thin sections have been extracted by FIB respectively under a facet and within the granular region (see Figs. 6 and 7).

On the TKD images of Fig. 6c it can be seen that a unique grain is present below a facet, even if the latter is not completely flat. With this method of analysis, however, only the intersection of the facet plane with the plane of the FIB foil can be determined but not the crystallographic plane of the facet itself. Two other methods have been used to try to determine the crystal indices of the facet normals: (i) the quantitative tilt fractographic method used by Sinha et al. [36] and based on [37] and (ii) direct EBSD measurements on the facets within the fracture surfaces. The results obtained on nearly ten facets and summarized in [17], did not show a unique direction for the facets normals. In our case, however, both methods suffered from relatively large experimental uncertainties due to the very small size of the facets and the accuracy of specimen positioning in the SEM.

The microstructure below the fracture surface within the granular region is shown on Fig. 7. On this figure the TKD technique reveals a micrometer thick layer (1 µm to 2 µm) containing some very small grains with a typical size ranging from 0.15 µm to 1 µm. This size is 10 to 100 times smaller than the average grain size of the original material. This suggests, therefore, that the presence of those grains might be due to the cyclic loading and to the presence of the fatigue crack as already mentioned in this material [1]. As can be seen on Fig. 7, the size of these small grains is not uniform and no preferred location of the smaller grains immediately beneath the fracture surface has been observed. Within this region of nanograins some nanopores were also observed (Figs. 7e and 7f.)

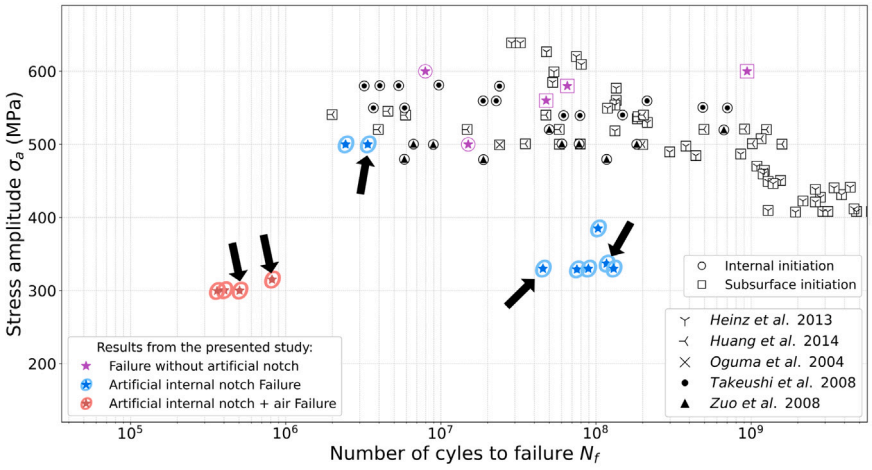

Fig. 3. SN curves (from [16]). The samples studied in this work are shown by arrows.

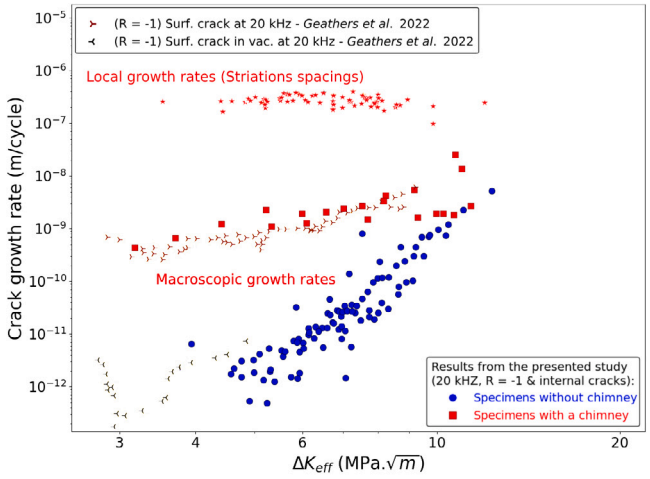

Fig. 4. Propagation curves for cracks propagating in vacuum and in air.

3.2. Fatigue specimens with chimney

All the specimens containing an internal notch connected with ambient air failed from a crack initiated at the notch with fatigue lives shorter than those of the notched specimen without a chimney at the same stress level as shown in Fig. 3. The crack growth rates $da/dN = f(\Delta K)$ curves were close to those measured in air at the same frequency by Geathers et al. [35] as shown in Fig. 4. Close to the notch, the fracture surface exhibited a very faceted area (called *Black Area* hereafter because it appeared very dark in the Optical Microscope (OM)) surrounded by a very bright zone (in the OM) formed of relatively planar features with a leaf-like aspect already described by Pilchak et al. [38] and A. Junet [39] in the same alloy . This aspect has been interpreted as a so-called *low ΔK faceted growth* mechanism occurring when the crack propagating on a given basal plane reaches a new grain where the basal plane has a different spatial orientation [38].

Fig. 8 shows the microstructure below the fracture surface within the *Black* and *Bright Areas*. This figure shows that, at a mesoscopic scale (~ 10 to 20 grains), only subtle differences between the two zones could be revealed by EBSD below the fracture surface. Grains in the black area seem to have a preferential orientation with the direction parallel to the direction of crack propagation. Looking to the 3D orientation of each hexagonal unit cells, there is no clear correlation between crystal orientation and crack propagation. The orientations of the grains in the bright area appear to be more random even if the statistics remain low. However, when looking at the 3D orientation of each hexagonal unit cell, it is tempting to correlate the fracture plane of each grain with the prismatic plane. At a more local scale, more important differences appear as shown in the following.

A thin foil has been extracted by FIB within the bright area where extensive striation was observed (Fig. 9). Fig. 9b and Fig. 12, show that, in this region of the fracture surface, the crack crossed nine grains (one β grain and 8 α grains), five of them containing striations. In the latter, SEM (Fig. 9) and TEM observations (Fig. 10) reveal marks with a wedge shape oriented in the direction of the crack propagation.

Fig. 10b shows a dark field TEM image of selected microstructural marks obtained by selecting a diffraction angle that is not present in the grain's diffraction pattern. Fig. 10c displays nano beam diffraction patterns of a family of marks (in red) and of the parent grain in which it is located (in yellow). A 87° misorientation is measured between these two matrixes. This value is very close to the 85° rotation around $[11\bar{2}0]$ mentioned in the literature to describe tensile $\{10\bar{1}2\}$ twin and already reported for the same alloy [40]. The fact that the wedge marks correspond to tensile twins has been confirmed by a TKD analysis of the same region as the one investigated by TEM. The result of this analysis is illustrated in Fig. 11 where the rotation of the CP cell between the wedge marks and the surrounding grains is also shown.

The lengths of the twins in the interior of the analyzed grains range from 200 to 600 nm and their thickness varies between 20 and 80 nm. The average angle ζ between the direction of the twin planes and the crack average surface is equal to 60° (Fig. 10a). The distance between two twins (0.24 μm) matches very well the mean value of the inter-striation distance obtained from Fig. 9a, (0.24 ± 0.02 μm), in the same grain, but, interestingly, this last value is much larger than the thickness of the twins.

Fig. 12 gives an overview of the presence — or the absence — of twins in the different grains observed within the thin foil. By comparison with the fracture surface of Fig. 9 it can be observed that the grain orientation has a strong influence on the formation of striations. When the latter are observed twins are systematically detected below the surface. As a corollary, within the grains without striation/twin the crack surface looked less smooth with more pronounced local deviations of the cracks surface (see the zones circled in green in Fig. 9).

Finally, the differences in fracture surfaces reported above between specimens with or without a chimney vanished when the cracks were long enough to enter into the external region of the *Fish-Eye* zone (ΔK larger than approximately 10 MPa.$\sqrt{m}$ [16]). This is illustrated in Fig. 13.

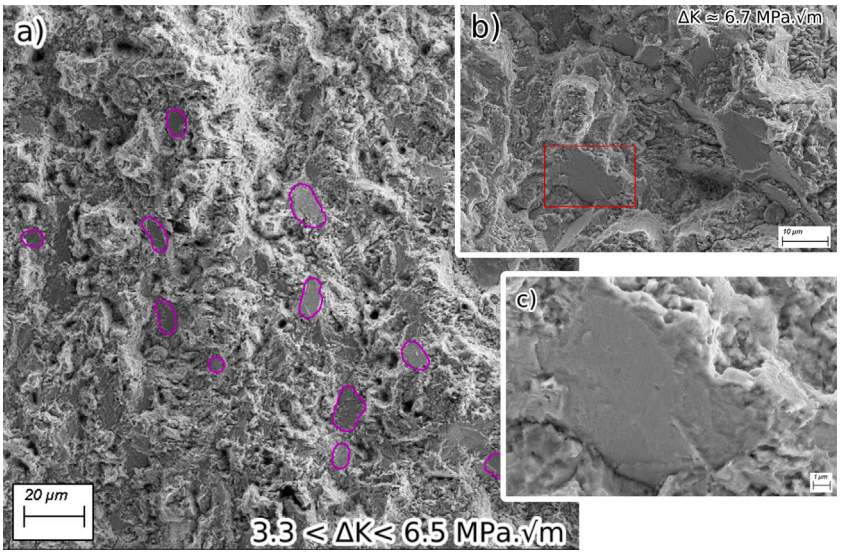

Fig. 5. SEM observations in the *Rough Area* of a Specimen without chimney cycled at 337 MPa during 4.55×10^7 cycles (a) Global view showing a "granular" aspect with scattered facets (circled in purple). (b) Enlarged view showing the "granular" aspect and some facets at higher magnification. (c) Enlarged view of the facet shown in the red rectangle in b).

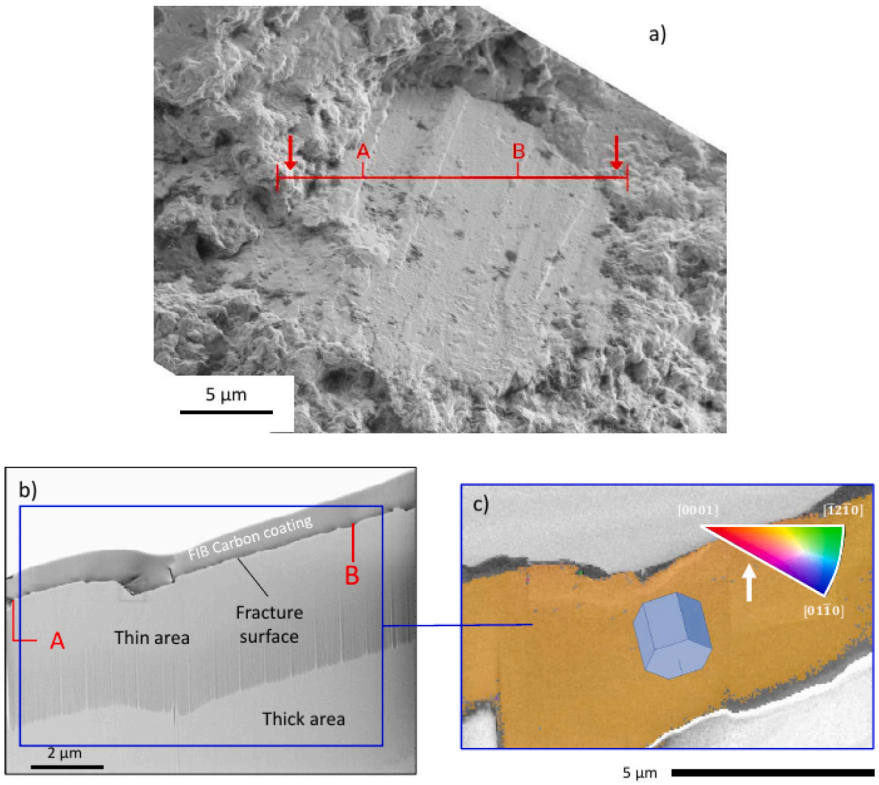

Fig. 6. SEM analysis of a facet located in the *Rough Area* of a specimen without chimney cycled at 337 MPa during 1.17×10^8 cycles. The red line in (a) indicates the thin foil position within the facet. (b) SEM image of the foil after extraction. A region of this lamella was thinned to enable TKD and TEM analysis. (c) TKD image corresponding to the blue rectangle in (b) showing that a unique grain is present under the facet. The IPF shows the crystal orientation in the vertical direction of the picture (white arrow). The angle between the $\vec{c}$-axis and the loading direction (assumed to be along the white arrow direction) is about 35°. An hexagonal unit cell illustrates the 3D orientation of the sectioned facet.

4. Discussion

Yoshinaka et al. [7] have studied the propagation behavior of small surface cracks in Ti-6Al-4V in air at atmospheric pressure (~ 0.1 MPa) and in vacuum (10^{-4} Pa). These authors describe - for the cracks which propagated in air - an "angular and sharp aspect" close to the initiation site ($\Delta K \sim 6$ MPa.$\sqrt{m}$) surrounded by a "larger flat striated zone" (still visible at $\Delta K = 18$ MPa.$\sqrt{m}$). In the case of vacuum, a "granular and round aspect" is described in the vicinity of the initiation site, surrounded by a "flat zone without striation". Those observations are in very good agreement with the results reported in our investigations. The experimental conditions of the two studies differ however in several points: the cyclic frequency (60 Hz vs. 20 kHz) the load ratio (0.1 vs. -1) and the stress state at the crack tip (plane stress evolving toward

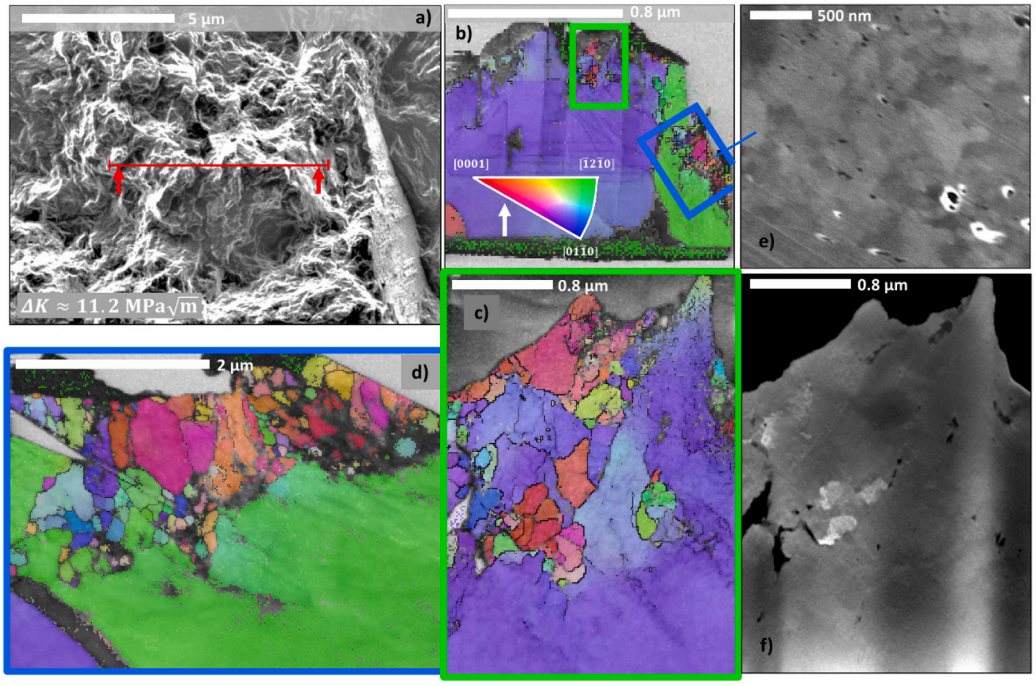

Fig. 7. Microstructure characterization below the fracture surface within the granular region of a specimen without chimney cycled at 337 MPa during 1.17×10^8 cycles. (a) SEM imaging of the fracture surface in a granular area. The localization of a wall extracted with FIB is represented by the red line and the surface of the thin lamella extracted at this point is indicated with the red arrows (ΔK = 5.9 MPa.m$^{1/2}$). (b) Overall TKD map of the thin lamella extracted perpendicular to the crack plane along the red line in (a) (pixel size: 100 nm). (c) and (d) TKD maps acquired with a pixel size of 15 nm (location shown respectively in the green and blue boxes of b) showing a nanograins layer just under the granular features of the crack surface (the grain size of the original material is 10 ± 1 µm). All TKD maps were indexed with the α titanium structure (no β phase detection) and exhibit IPF color coding for the vertical (loading) direction of the maps (white arrow). (e) and (f) are respectively a SEM image in BSE mode and a HAADF-STEM image of the thin foil at nanograins level. Both images show the presence of nanopores within this nanostructured layer (dark spots).

plane strain vs. plane strain). This tends to indicate, surprisingly, that the deformation mechanisms at the crack tip do not seem to depend strongly on those parameters.

4.1. Sample without chimney

Within the RA, the extracted thin foil allowed us to confirm that a single grain is present below a facet even when it is not completely flat. This is in agreement with the so called "low ΔK faceted growth" suggested by Pilchak [5]. We did not find that the facets observed in the granular zone corresponded to the basal plane of the hexagonal unit cell as sometimes reported in this material [36,41]. This could be due to the small facet size which, in our case, led to relatively large experimental uncertainties in the methods used for determining the facets normals. Another explanation could be the presence, in the alloy investigated here, of macrozones (see Section 2, Fig. 2). Evenaerts et al. [6] have shown in a study of Ti-6Al-4V wires that the material texture has a strong influence on the type of planes along which the facets form.

The TKD analysis has enabled us to visualize the size and shape of the very small grains formed beneath the fracture surface. Hong & Sun [1] have observed a thin foil extracted by FIB out of the fractographic surfaces of a high-strength steel and a Ti-6Al-4V alloy which have been ultrasonically fatigue tested. TEM observations revealed the presence of nanograins in a micrometer-thick layer under the crack surface [1]. Nano grains were also directly observed in specimens of Ti-6Al-4V produced by Selective Laser Melting (SLM) using precession electron diffraction [42]. Su et al. [12] observed the same type of microstructure in a bi-modal Ti-6Al-4V alloy for which different loading ratios were tested. In the RA the nanograin layer was detected in specimens cycled at $R = -1$ but not at $R = 0.5$. Hong & Sun [1] also reported an absence of RA for specimens ultrasonically cycled at $R = -1$ which failed after a short amount of cycles ($N = 1.28 \times 10^5$ cycles). In that case, the size of the RA was reduced but still present for specimens cycled at $R = 0.1$.

According to Hong et al. [43] these observations confirm that the nanograins are formed by the so-called Numerous Cyclic Pressing (NCP) model: an accumulation of plastic deformation originating from the repeated contact and pressing between the two crack lips. In this model, the formation of the RA and of the nanograins layer is favored by long fatigue lives and negative loading ratios. Another formation mechanism of the RA and of nanograins has been proposed by Oguma et al. [4] who suppose that the repeated contact of the internal crack surfaces induces a cold-welding phenomenon. The cyclic loading provokes a repeated fracture of the cold-welded surfaces (not necessarily at the same location within the grains) leading to some microstructure refinement. Cold-welding provoked by cyclic loading has been experimentally observed by in situ TEM observations of platinum fatigue specimens containing nanocrystals [44].

Our results show that bringing air molecules to an internal crack during its propagation seems to hinder the formation of both a granular area and of nanograins. This was already observed by Oguma et al. [4] on long surface cracks in CT specimens. The presence of oxygen or hydrogen molecules can alter the plasticity mechanisms in Ti-6Al-4V alloys in many complex ways (see [45] for a recent review). As pointed out by Oguma and Nakamura [4], a key effect of oxygen is that it creates a thin oxide layer at the surface of the crack hindering the cold welding process. Grain refinement according to the NCP model should in principle be active both in air and in vacuum and cannot therefore account for the absence of nanograins in presence of air, unless the nanometric oxide layer [46] is being constantly broken by the repeated contacts of the crack surfaces. Our TEM and SEM observations have shown the presence of nanopores within the nanograin layer (Fig. 7). Similar nanopores have also been reported by Oguma [47] in a region of nanograins obtained during uniaxial compression tests in Ti-6Al-4V in vacuum. According to this author, the nanopores result from an imperfect cold welding process.

The fact that nanograins do not form in the presence of air could however be also explained in the frame of the NCP model [43]. For

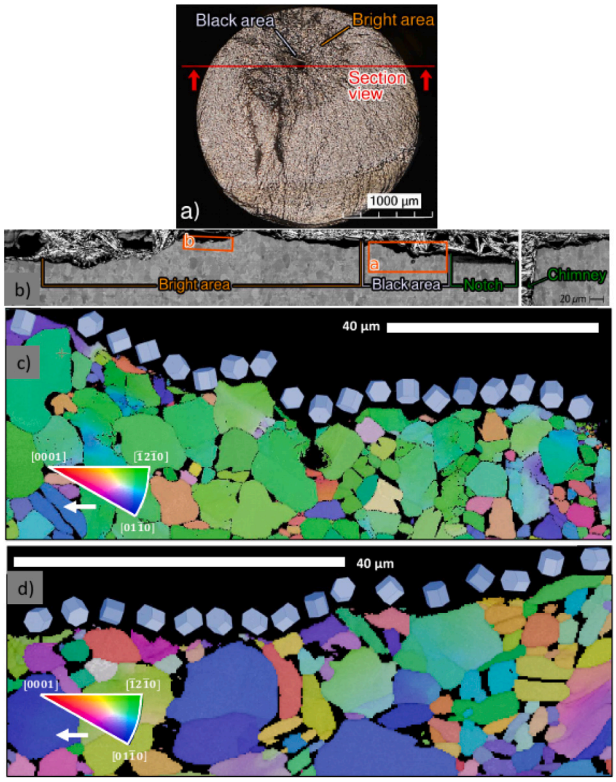

Fig. 8. Broad Ion Beam (BIB) cross-section perpendicular to the average crack plane for a specimen with a chimney cycled at 315 MPa during 8.16×10^5. (a) Optical imaging of the fracture surface and location of the cross-section through the notch and the dark and bright areas. (b) SEM picture of the BIB section observed in backscattered electron mode to distinguish the microstructure under the fracture surface around the internal notch. The notch and the chimney are represented in green, Black Area is located in white and Bright Area, in orange. Two EBSD maps obtained in the black and bright areas are shown in (c) and (d) respectively. Both maps are located within the orange rectangles in (b) and were obtained with a step size of 200 nm. The IPFs show the crystal directions parallel to the direction of crack propagation (white arrow). On these maps, the black regions correspond to the detection of the β phase. For every α grain on the surface, hexagonal unit cells are superimposed on the maps.

samples with a chimney the fatigue lives are much shorter than without: $\sim 10^6$ *v.s.* $\sim 10^8$ cycles (see Fig. 3). Thus, in the former case, the plastic strain accumulation due to repeated contacts at the crack surfaces might not be large enough to induce the formation of the nanograins. The results obtained in this work cannot help to decide between the two models/mechanisms.

4.2. Sample with chimney

The presence of the chimney which carries air molecules to the crack tip has a strong influence on the crack tip mechanisms. The granular areas containing facets observed in vacuum have been replaced by a faceted fracture surface where striations can be observed when $\Delta K > 5$ MPa.$\sqrt{\text{m}}$ [16].

The inter-striation spacing has been used to locally estimate the crack growth rate assuming propagation between two striations during one loading cycle. Ten measurements have been carried out per specimen at ΔK values ranging from 4 to 10 MPa.$\sqrt{\text{m}}$. Within this range, the crack growth rate does not seem to vary with ΔK values, its average value is $2.7\times10^{-7} \pm 1.0\times10^{-7}$ m/cycle (*cf.* Fig. 4). Our measurements are in good agreement with those of Yoshinaka et al. [7], also based on striation spacing, who measured crack growth rates around 1.4×10^{-7} m when $\Delta K = 18$ MPa.$\sqrt{\text{m}}$ for a crack propagating in air environment in the same alloy loaded in tension at $R = 0.1$ [7].

The "*averaged*" macroscopic crack growth rate has also been estimated thanks to tomography data for the specimens with a chimney [16] giving values that are two orders of magnitude lower. A possible explanation for this discrepancy has been given by Williams et al. [48] who suggest that propagation might not be homogeneous along the crack front so that the macroscopic crack growth rate - which is an averaged value - can differ from the local one. Another explanation might be that, in the regions with striations, the crack stays arrested during several cycles (between 10 and 100) before propagating again.

Based on the position of the thin foil within the fracture surface ($\sim$ 320 µm from the notch tip), an estimation of the SIF range at which the twins observed on Fig. 9 were created can be calculated [16]. This value ($\sim$ 6.1 MPa.$\sqrt{\text{m}}$) can be used to calculate a rough approximation of the reverse cyclic plastic zone size, $r_{p,cycl}$, at the crack tip (plane strain assumption):

$$r_{p,cycl} = \frac{(1-2\nu)^2}{\pi}\frac{\Delta K_I^2}{4\sigma_Y^2} \quad (1)$$

In the region of the twins, a value of 500 nm is obtained for $r_{p,cycl}$ which is of the same order of magnitude than the length of the twins (from 200 to 600 nm). This tends to indicate that the presence of a twin is correlated to the plastic activity at the crack tip.

Chi et al. [49] have studied tensile twinning in Ti-6Al-4V; they claim that twin nucleation occurs in α grains when the plastic strain reaches a certain level. One might assume, therefore, that in our case, the crack stays arrested until enough cyclic plasticity is accumulated to trigger the formation of a twin.

As a matter of fact, twinning during fatigue of Ti-6Al-4V has already been reported in several studies but, to the best of our knowledge, it has never been related to striations. For example, Lavogiez et al. [40] observed that tensile-twinning occurs at the surface of a cycled specimen. When slip bands try to pass from a soft grain (*i.e.* whose orientation is favorable for slip with a high Schmid factor [50]) to a neighboring hard grain (*i.e.* low Schmid factor), they do so by forming a twin in the latter. Also, Ma et al. [51] studying a lamellar Ti-6Al-4V alloy reported tensile-twinning in the grains near a fatigue crack. In this study, Schmid factor calculations showed that $\{10\bar{1}2\}$ tensile-twinning principally occurred in grains with low values of the Schmid factor of the basal slip system. In other words, for those authors, when the $\vec{c}$ -axis is aligned with the loading direction, twinning tends to be favored because basal slip is difficult to trigger. This interplay between $\vec{c}$ -axis direction and twinning occurrence is also claimed by Chi et al. [49].

Conversely, Sun et al. observed during fatigue of a Ti-6Al-4V alloy that $\{10\bar{1}2\}$ tensile-twinning occurred in grains with high Schmid factor for basal slip [52]. In this case, the authors claim that high stress levels provoke dislocation accumulation in some grains until a point when twinning is triggered to accommodate the plastic strain.

Munroe et al. [53] report that the presence of twinning in titanium can be observed in grains with $\vec{c}$ -axis aligned with the loading direction but also in the case of high Schmid factors for basal slip. In this paper, different results from several studies are listed and show that $\{10\bar{1}2\}$ twinning was dominant in titanium single crystals if the Ω angle between the $\vec{c}$ -axis and the loading direction was equal to 12°, 30°, close to 0° or between 30° and 40°. Fig. 12 summarizes the presence — or the absence — of twins in the different grains observed in the thin foil extracted by FIB. On this figure, it can be seen that tensile-twinning is not observed in the grains with a $\vec{c}$ -axis almost aligned with the loading direction and twinning marks are present when 37° $< \Omega <$44°.

To try to rationalize the presence of tensile-twinning, a Schmid factor analysis [54] has been carried out for the three grains labeled with the "*" symbol observed in Fig. 12. Rather than assuming a uniaxial stress state in the loading direction, the triaxial stress field at the crack tip is estimated by Finite Element (FE) calculation using a 2D mesh containing a crack under plane strain (to account for the fact

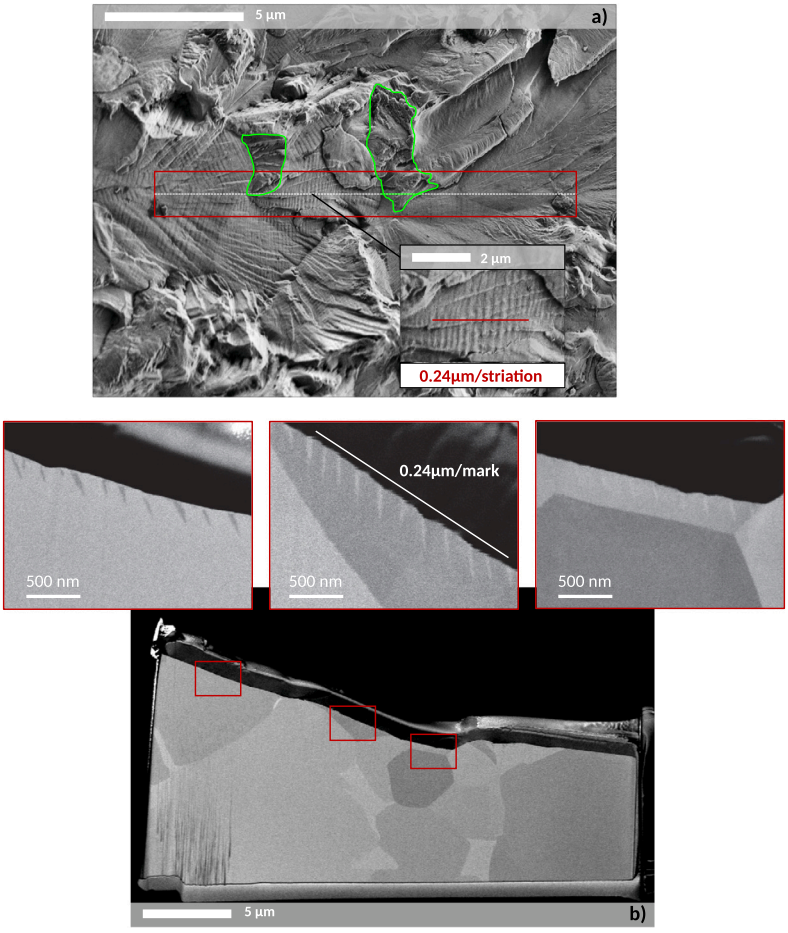

Fig. 9. (a) SEM picture representing a striated zone in the Bright Area from the fracture surface of a specimen with chimney cycled at 300 MPa during 5.04×10^5 cycles. The localization of the wall extracted with FIB is represented by the white dotted line. The insert zooms in on the striation and allows to measure an inter striation spacing of 0.24 µm. Areas without striations in the plane of the thin foil are circled in green. (b) Low voltage SEM pictures in BSE mode of the extracted wall located under the striated zone depicted in (a). The inserts zoom in on marks seen under the striations. The distance between two marks (0.24 µm) matches very well the inter-striation spacing obtained from (a) meaning that one mark is present under each striation. The crack propagates from left to right.

that cracks are internal) (*cf.* Fig. 14a). The crack in the mesh is slightly inclined (20 degrees) to be more representative of the experimental observations (assuming a nearly vertical loading in Fig. 12). The FE calculation is performed with the assumption of an homogeneous, isotropic, linear elastic material given the low level of the remote stress with respect to the material's yield strength.

Then, for the three grains shown on the left of Fig. 12 (marked with the * symbol) the obtained FE stress field, averaged over ten elements, at the crack tip is used to calculate a resolved shear stress, τ^s, for each slip system s listed in Table 2.

$$\tau^s = \boldsymbol{b}^T \bar{\bar{\sigma}} \boldsymbol{n} \tag{2}$$

with $\boldsymbol{n}$ the slip plane normal unit vector, $\boldsymbol{b}$ the unit vector orienting the slip direction and $\bar{\bar{\sigma}}$ the stress tensor.

In a similar approach to slip, deformation twinning can be described by an homogeneous shear parallel to the twinning plane (normal **n**) in the twinning direction **b** [55,56]. This "slip approach" is also applied to the twin mechanisms to obtain an equivalent shear rate. This approach has been carried out for the tensile and compressive twinning systems listed in Table 2. However, contrary to slip modes, the twin modes are uni-directional. Therefore, only positive resolved shear stresses on the specified twin systems might activate deformation twinning in the grain and result in a twin lattice that is indeed a mirror of the parent grain lattice in the twinning plane.

Table 2
Families of slip and twin systems used in the Schmid factors analysis. The twinning planes and directions for the tensile and compressive twins correspond to a description of deformation twinning as an homogeneous shear, similar to slip but uni-directional.

Slip mode	Slip plane	Slip direction	Nb. of equiv. syst.
Basal	(0002)	$< 11\bar{2}0 >$	3
Prismatic	$\{10\bar{1}0\}$	$< \bar{1}2\bar{1}0 >$	3
Pyramidal $< c+a >$	$\{10\bar{1}1\}$	$< \bar{2}113 >$	12
Twinning mode	**Twinning plane**	**Twinning direction**	**Nb. of equiv. syst.**
Tensile	$\{10\bar{1}2\}$	$< \bar{1}011 >$	6
Compressive	$\{11\bar{2}2\}$	$< 11\bar{2}\bar{3} >$	6

The Critical Resolved Shear Stress (CRSS) for the different slip systems in titanium have been computed from several studies as reported by Castioni et al. [57] and summarized in Table 3. For the twinning systems, as a first approach, the CRSS have been taken equal to the value of the "harder" system, *i.e.* the $\langle c+a \rangle$ pyramidal slip system in the case of Ti-6Al-4V according to Bridier et al. [58].

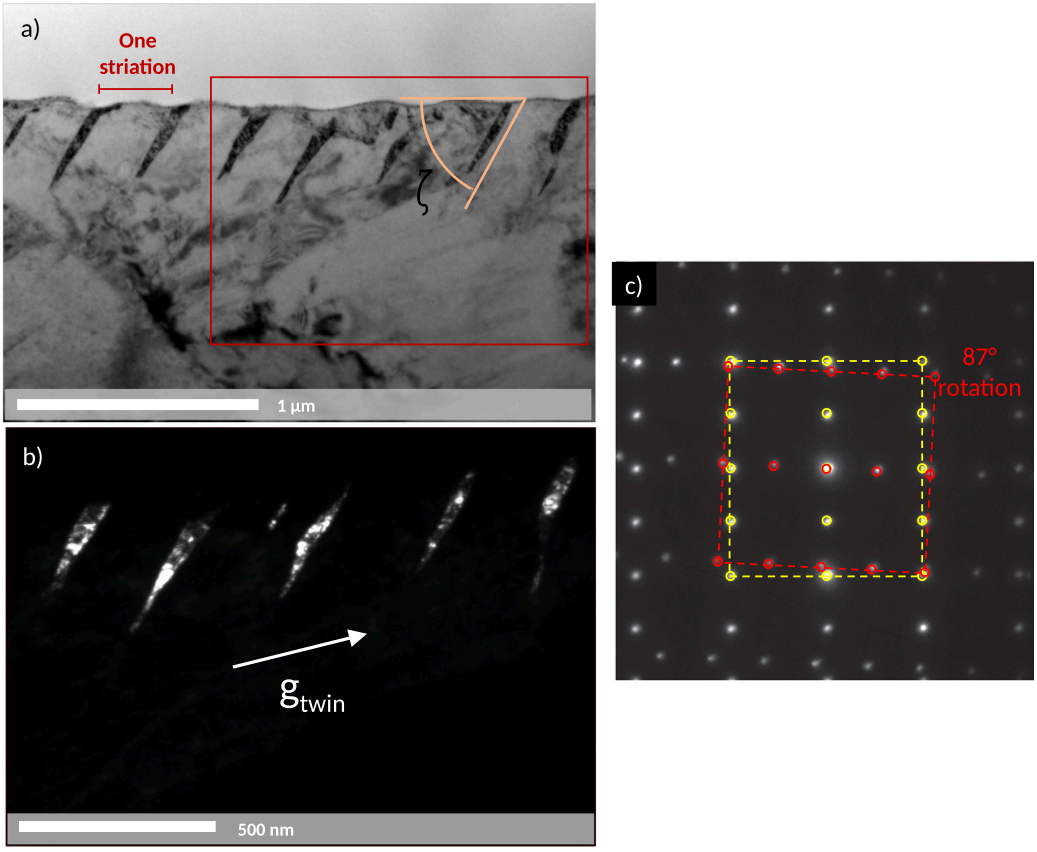

Fig. 10. (a) bright-field TEM image of the marks. ζ is the average angle between the direction of the marks and the crack average surface (the crack propagates from right to left). (b) Dark field TEM image of microstructural marks obtained by selecting a diffraction angle that is not present in the parent grain's diffraction pattern. (c) Nano beam diffraction patterns of a microstructural mark (in red) and of the parent grain in which it is located (in yellow). A 87° misorientation is measured between the two patterns which is very close to that of a tensile-twinning relation in titanium (85°). The crack propagation direction is from right to left.

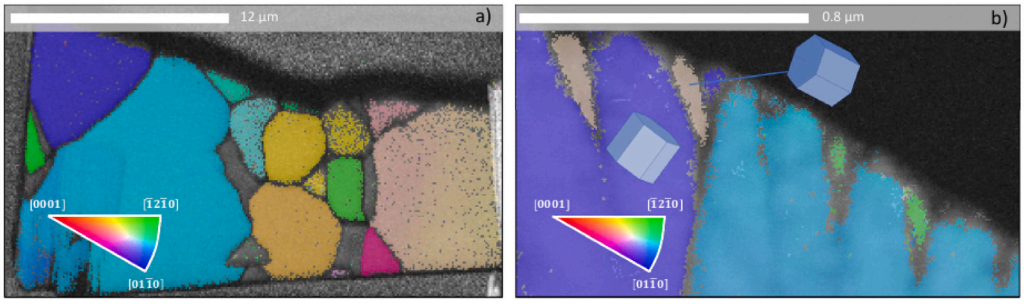

Fig. 11. Orientation maps of the extracted wall located under the striated zone (a) EBSD analysis of the extracted lamella as a whole, shown in Fig. 9. (b) detailed view of the twinning marks for two adjacent grains. (b) TKD picture (step size: 5 nm). The IPF presents the crystal direction normal to the pictures. The crystal misorientation between the marks and the bulk corresponds to the tensile-twinning relation.

Table 3
Relative critical resolved shear stresses used in the Schmid factor analysis for the different families of slip and twin systems. The values are normalized by the lowest CRSS (corresponding to the prismatic slip). Extracted from the work of Bridier et al. [58].

τ_c^{prism}	τ_c^{basal}	$\tau_c^{pyr<c+a>}$	τ_c^{Ttwin}	τ_c^{Ctwin}
1.0	1.14	1.59	1.59	1.59

To predict which slip or twin system is activated for each crystallographic orientation, the calculated resolved shear stress, τ^s, is normalized by the CRSS, τ_c^s, to obtain a shear rate $\dot{\gamma} = \dot{\gamma}_0 |\tau^s/\tau_c^s|^{1/m}\ sign(\tau^s)$ with $\dot{\gamma}_0$ a reference slip rate and m a strain-rate sensitivity exponent (as detailed in [59] — Appendix A). The "preferential" deformation mode is obtained by comparing the maximum shear rate in each slip or twin systems. The results of this analysis are shown in Fig. 14b. It can be seen on this figure that twinning is predicted in the grain labeled ** but not in the two others (labeled * and ***). The results of the simulation are therefore the *opposite of what has been experimentally observed* but they are in good agreement with the observation of Ma et al. [51] and Chi et al. [49] who observed that twin is favored when the local $\vec{c}$ -axis is perpendicular to the loading direction.

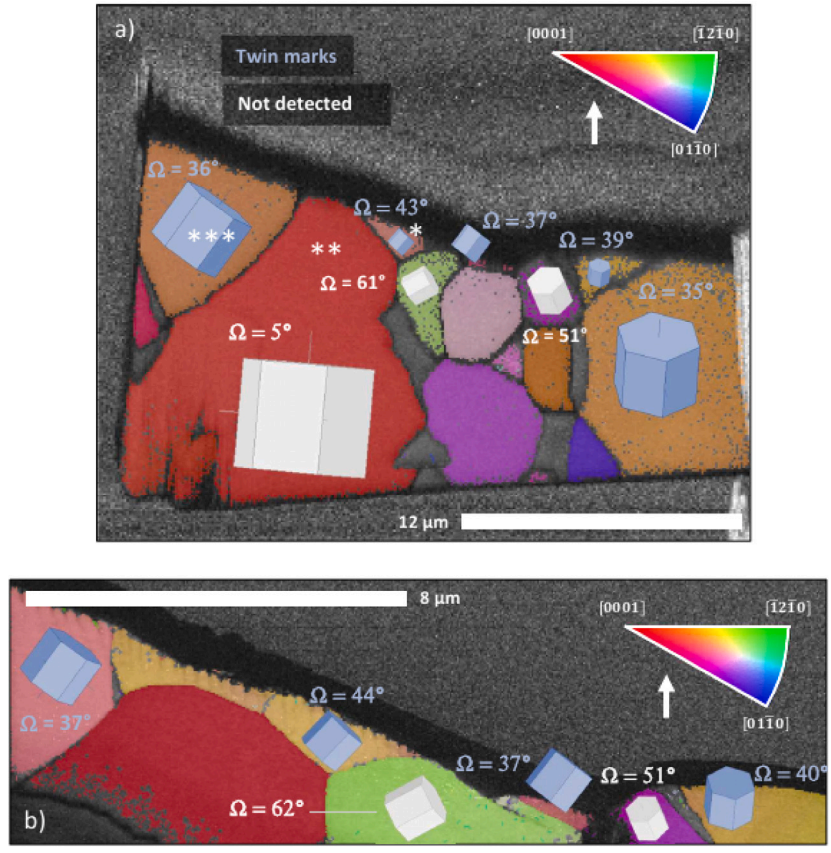

Fig. 12. Summary of the presence of striations and of the angle between $\vec{c}$-axis and vertical loading direction for each grain located in the extracted wall which is represented in Fig. 9. (a) Low magnification TKD map (Step size: 100nm). (b) Detailed TKD map (step size 40nm) of (a) after a supplementary polishing session using a precision ion polishing system (PIPS II, Model 695, Gatan Inc.). The IPF shows the crystal direction parallel to the vertical direction of the picture (assumed to be approximately the loading direction). Ω is an estimation of the angle between the $\vec{c}$-axis and the loading direction. Grains whose orientation has not been represented have been indexed with β titanium structure. Almost all surface grains present striations with the exception of 3 grains. The Schmid factors of the three grains with "*" markers have been analyzed.

To try to understand the discrepancies reported above between experiment and simulation one has to bear in mind that the prediction of the Schmid factor approach strongly relies on the respective values of CRSS. These values can be identified experimentally for easy slip modes such as basal and prismatic slip, but require more elaborate strategies for twinning systems. It is also known, for titanium, that the interstitial content has some influence on the respective values of the CRSS. Increasing the oxygen interstitial content in Ti leads to an increase of the CRSS values for basal and prismatic slip and this effect is more pronounced for prismatic slip [60]. In the work presented here, it was observed that the environment has also a strong influence on the crack tip deformation mechanisms as the twins are only observed when air (and in particular oxygen) is present. As far as we know, however, the effect of the oxygen interstitial content on the CRSS value required for twinning is not known. Obtaining this type of data would be a prerequisite before performing any simulation for predicting the observed twinning mechanism at the crack tip.

5. Conclusion

This paper presents a detailed analysis of fatigue mechanisms occurring in Ti-6Al-4V specimens containing a controlled internal sharp defect. The fatigue tests (described elsewhere [16]) have been carried in the HCF ($N_R \sim 10^5$ cycles) and the VHCF ($N_R > 10^7$–10^8 cycles) regimes. All specimens broke from the propagation of an internal crack initiated from the artificial defect with significantly shorter fatigue lives (~ 2 decades) when internal defects were connected to the specimen surface allowing ambient air to reach the crack tip.

The findings of this study can be summarized as follows:

- The microstructure present below the fracture surface of the broken specimens has been studied by electron microscopy (SEM, EBSD, TKD and TEM).
- The formation of nanograins and nanopores was observed below the surface of cracks growing in vacuum but not in cracks connected with ambient air.
- Below the surface of internal cracks growing in air, large regions containing striations were observed, whereas no striation were observed on the specimens with internal cracks without contact with air and loaded at approximately the same load level.
- The presence of a striation is associated to the formation of a tensile twin below the surface of the crack.

CRediT authorship contribution statement

Louis Hébrard: Writing – review & editing, Visualization, Validation, Methodology, Investigation, Formal analysis, Data curation, Conceptualization. **Thierry Palin-Luc:** Writing – review & editing, Validation, Supervision, Project administration, Methodology, Formal analysis, Conceptualization. **Nicolas Ranc:** Writing – review & editing, Validation, Methodology, Investigation, Formal analysis, Conceptualization. **Arnaud Weck:** Writing – review & editing, Resources. **Thierry Douillard:** Writing – review & editing, Resources, Investigation. **Nicholas Blanchard:** Writing – review & editing, Resources, Investigation. **Sylvain Dancette:** Writing – review & editing, Resources,

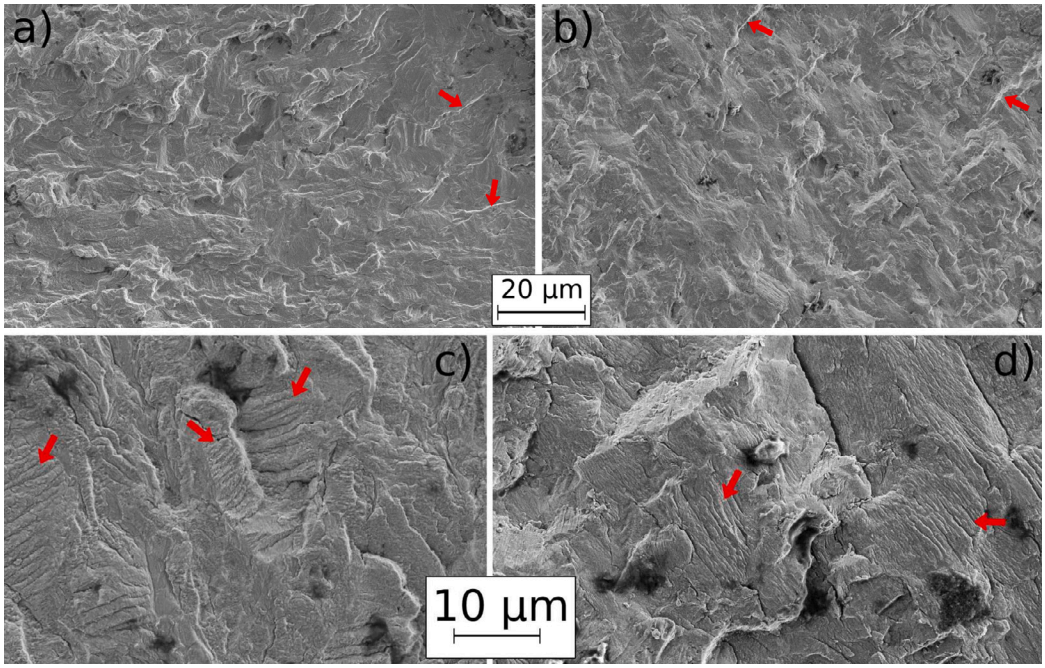

Fig. 13. Fractographic aspect of the external area of the *Fish-Eye* zone observed with SEM for specimens with (b & d) and without (a & c) a chimney. Low magnification pictures (a & b) show that the fracture surface presents a combination of rough and planar zones (the latter being less planar than the facets) with many step lines (*cf.* red arrows). Also, a higher magnification (c & d) allows to remark the presence of ridges in the external area of the *Fish-Eye* zone (also located by red arrows) for the two types of specimen. (a) $\Delta K \approx 11.2$ MPa.$\sqrt{\text{m}}$ Specimen without chimney cycled at 337 MPa. (b) $\Delta K \approx 10.1$ MPa.$\sqrt{\text{m}}$ Specimen with chimney cycled at 315 MPa. (c) $\Delta K \approx 12.4$ MPa.$\sqrt{\text{m}}$ Specimen without chimney cycled at 500 MPa. (d) $\Delta K \approx 10.9$ MPa.$\sqrt{\text{m}}$ Specimen with chimney cycled at 315 MPa.

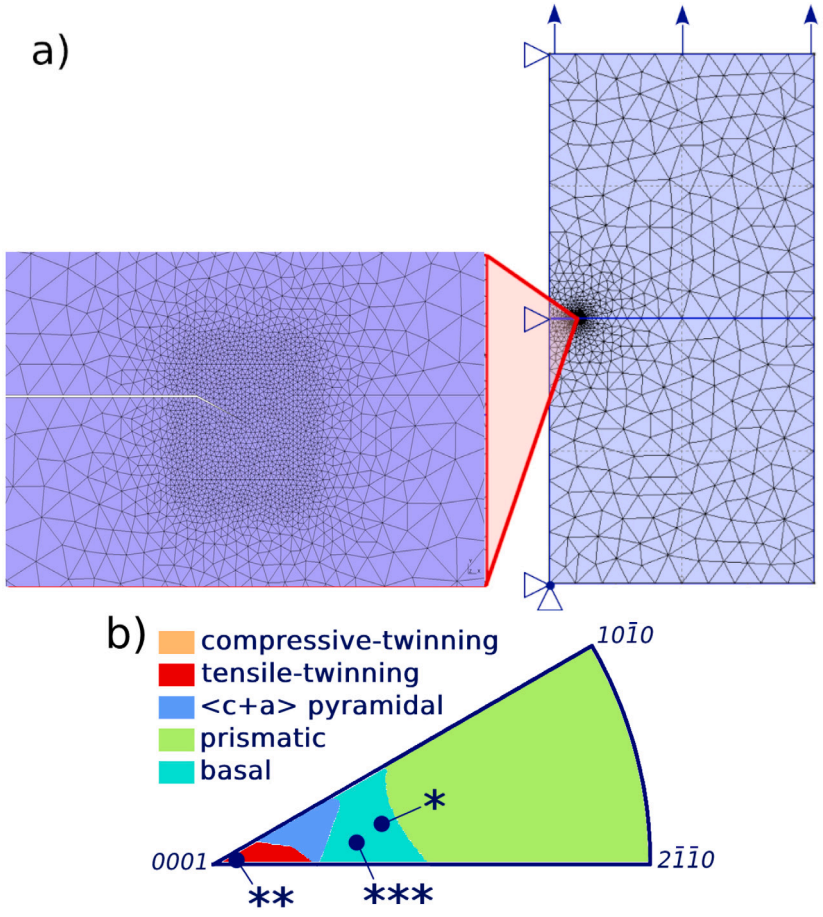

Fig. 14. (a) 2D model used for the elastic finite element calculation carried out to obtain the stress field at the crack tip (b) Deformation system activated for each microstructure orientation according to the Schmid factor analysis. The * markers correspond to the three grains indexed by similar markers in Fig. 12.

Investigation. **Jean-Yves Buffiere:** Writing – original draft, Validation, Supervision, Project administration, Methodology, Investigation, Funding acquisition, Formal analysis, Data curation, Conceptualization.

Declaration of competing interest

The authors declare that they have no known competing financial interests or personal relationships that could have appeared to influence the work reported in this paper.

Acknowledgments

The authors acknowledge the European Synchrotron Radiation Facility and the Soleil Synchrotron Facility for provision of beamtime at beamline ID19 and Psiche, respectively. The authors express their gratitude to F. Mercier for his valuable assistance for SPS diffusion bonding, to Andrew King from Soleil and Marta Majkut from ESRF for their assistance during the synchrotron experiments. Thanks are also due to the CLyM (Consortium Lyon Saint-Etienne de Microscopie: http://www.clym.fr) supported by the CNRS, the "Grand Lyon" and the Rhône-Alpes Region for the use of the Zeiss NVision40 FIB/SEM.

Data availability

Data will be made available on request.

References

[1] Hong Y, Sun C. The nature and the mechanism of crack initiation and early growth for very-high-cycle fatigue of metallic materials – An overview. Theor Appl Fract Mech 2017;92:331–50. http://dx.doi.org/10.1016/j.tafmec.2017.05.002, URL: https://linkinghub.elsevier.com/retrieve/pii/S0167844217301581.

[2] McEvily A, Nakamura T, Oguma H, Yamashita K, Matsunaga H, Endo M. On the mechanism of very high cycle fatigue in Ti–6Al–4V. Scr Mater 2008;59(11):1207–9. http://dx.doi.org/10.1016/j.scriptamat.2008.08.012, URL: https://linkinghub.elsevier.com/retrieve/pii/S1359646208006088.

[3] Liu X, Sun C, Hong Y. Effects of stress ratio on high-cycle and very-high-cycle fatigue behavior of a Ti–6Al–4V alloy. Mater Sci Eng A 2015;622:228–35. http://dx.doi.org/10.1016/j.msea.2014.09.115, URL: https://linkinghub.elsevier.com/retrieve/pii/S0921509314012313.

[4] Oguma H, Nakamura T. Fatigue crack propagation properties of Ti–6Al–4V in vacuum environments. Int J Fatigue 2013;50:89–93. http://dx.doi.org/10.1016/j.ijfatigue.2012.02.012, URL: https://linkinghub.elsevier.com/retrieve/pii/S0142112312000734.

[5] Pilchak AL, Williams JC. Observations of facet formation in near-α titanium and comments on the role of hydrogen:. Metall Mater Trans A 2010;42A:1000–27.

[6] Everaerts J, Verlinden B, Wevers M. Investigation of fatigue crack initiation facets in Ti-6Al-4V using focused ion beam milling and electron backscatter diffraction: Investigation of crack initiation facets. J Microsc 2017;267(1):57–69. http://dx.doi.org/10.1111/jmi.12547, URL: https://onlinelibrary.wiley.com/doi/10.1111/jmi.12547.

[7] Yoshinaka F, Xue G, Fujimura N, Nakamura T. Effect of vacuum pressure on small crack propagation in Ti-6Al-4V. Int J Fatigue 2021;142:105961. http://dx.doi.org/10.1016/j.ijfatigue.2020.105961, URL: https://linkinghub.elsevier.com/retrieve/pii/S014211232030493X.

[8] Sakai T, Nakagawa A, Oguma N, Nakamura Y, Ueno A, Kikuchi S, et al. A review on fatigue fracture modes of structural metallic materials in very high cycle regime. Int J Fatigue 2016;93:339–51. http://dx.doi.org/10.1016/j.ijfatigue.2016.05.029, URL: https://linkinghub.elsevier.com/retrieve/pii/S0142112316301372.

[9] Jiang Q, Sun C, Liu X, Hong Y. Very-high-cycle fatigue behavior of a structural steel with and without induced surface defects. Int J Fatigue 2016;93:352–62. http://dx.doi.org/10.1016/j.ijfatigue.2016.05.032, URL: https://linkinghub.elsevier.com/retrieve/pii/S0142112316301402.

[10] Fu R, Zheng L, Ling C, Zhong Z, Hong Y. An experimental investigation of fatigue performance and crack initiation characteristics for an SLMed Ti-6Al-4V under different stress ratios up to very-high-cycle regime. Int J Fatigue 2022;164:107119. http://dx.doi.org/10.1016/j.ijfatigue.2022.107119, URL: https://linkinghub.elsevier.com/retrieve/pii/S0142112322003759.

[11] Heinz S, Eifler D. Crack initiation mechanisms of Ti6Al4V in the very high cycle fatigue regime. Int J Fatigue 2016;93:301–8. http://dx.doi.org/10.1016/j.ijfatigue.2016.04.026, URL: https://linkinghub.elsevier.com/retrieve/pii/S0142112316300809.

[12] Su H, Liu X, Sun C, Hong Y. Nanograin layer formation at crack initiation region for very-high-cycle fatigue of a Ti-6Al-4V alloy: Nanograin Formation for VHCF of TI Alloy. Fatigue Fract Eng Mater Struct 2017;40(6):979–93. http://dx.doi.org/10.1111/ffe.12562, URL: https://onlinelibrary.wiley.com/doi/10.1111/ffe.12562.

[13] Chang Y, Pan X, Zheng L, Hong Y. Microstructure refinement and grain size distribution in crack initiation region of very-high-cycle fatigue regime for high-strength alloys. Int J Fatigue 2020;134:105473. http://dx.doi.org/10.1016/j.ijfatigue.2020.105473, URL: https://linkinghub.elsevier.com/retrieve/pii/S0142112320300049.

[14] Murakami Y, Nomoto T, Ueda T, Murakami Y. On the mechanism of fatigue failure in the superlong life regime (N>107 cycles). Part 1: influence of hydrogen trapped by inclusions. Fatigue Fract Eng Mater Struct 2000;23(11):893–902. http://dx.doi.org/10.1046/j.1460-2695.2000.00328.x, URL: https://onlinelibrary.wiley.com/doi/abs/10.1046/j.1460-2695.2000.00328.x, _eprint: https://onlinelibrary.wiley.com/doi/pdf/10.1046/j.1460-2695.2000.00328.x.

[15] Li SX. Effects of inclusions on very high cycle fatigue properties of high strength steels. Int Mater Rev 2012;57(2):92–114. http://dx.doi.org/10.1179/1743280411Y.0000000008.

[16] Hebrard L, Buffiere J-Y, Palin-Luc T, Ranc N, Majkut M, King A, et al. Environment effect on internal fatigue crack propagation studied with in-situ X-ray microtomography. Mater Sci Eng A 2023;882:145462. http://dx.doi.org/10.1016/j.msea.2023.145462, URL: https://linkinghub.elsevier.com/retrieve/pii/S0921509323008869.

[17] Hébrard L. Study on the effect of the environment on internal fatigue crack propagation in Ti-6Al-4V [Ph.D. thesis], 2023, URL: http://www.theses.fr/2023ISAL0120. Thèse de doctorat dirigée par Buffière, Jean-Yves et Palin-Luc, Thierry Matériaux Lyon, INSA 2023.

[18] Lunt D. The effect of macrozones in Ti-6Al-4V on the strain localisation behaviour [Ph.D. thesis], The University of Manchester, United Kingdom; 2014.

[19] Junet A, Messager A, Boulnat X, Weck A, Boller E, Helfen L, et al. Fabrication of artificial defects to study internal fatigue crack propagation in metals. Scr Mater 2019;171:87–91. http://dx.doi.org/10.1016/j.scriptamat.2019.05.018, URL: https://linkinghub.elsevier.com/retrieve/pii/S1359646219302866.

[20] Junet A, Messager A, Weck A, Nadot Y, Boulnat X, Buffiere J-Y. Internal fatigue crack propagation in a Ti-6Al-4V alloy: An in situ study. Int J Fatigue 2023;168:107450. http://dx.doi.org/10.1016/j.ijfatigue.2022.107450, URL: https://linkinghub.elsevier.com/retrieve/pii/S0142112322007009.

[21] Luo Y, Wu SC, Hu YN, Fu YN. Cracking evolution behaviors of lightweight materials based on in situ synchrotron X-ray tomography: A review. Front Mech Eng 2018;13(4):461–81. http://dx.doi.org/10.1007/s11465-018-0481-2, URL: http://link.springer.com/10.1007/s11465-018-0481-2.

[22] Yoshinaka F, Nakamura T, Oguma H, Fujimura N, Takeuchi A, Uesugi M, et al. Characterization of internal fatigue crack initiation in Ti-6Al-4V alloy via synchrotron radiation X-ray computed tomography. Fatigue Fract Eng Mater Struct 2023;1–10. http://dx.doi.org/10.1111/ffe.13957, URL: https://onlinelibrary.wiley.com/doi/10.1111/ffe.13957.

[23] Xue G, Tomoda Y, Nakamura T, Fujimura N, Takahashi K, Yoshinaka F, et al. Detection of small internal fatigue cracks in Ti-6Al-4V via synchrotron radiation nanocomputed tomography. Fatigue Fract Eng Mater Struct 2022;2693–702. http://dx.doi.org/10.1111/ffe.13765, URL: https://onlinelibrary.wiley.com/doi/10.1111/ffe.13765.

[24] Messager A, Junet A, Palin-Luc T, Buffiere J-Y, Saintier N, Ranc N, et al. In situ synchrotron ultrasonic fatigue testing device for 3D characterisation of internal crack initiation and growth. Fatigue Fract Eng Mater Struct 2019;43.

[25] Zaefferer S. A critical review of orientation microscopy in SEM and TEM. Cryst Res Technol 2011;46(6):607–28. http://dx.doi.org/10.1002/crat.201100125, URL: https://onlinelibrary.wiley.com/doi/abs/10.1002/crat.201100125. _eprint: https://onlinelibrary.wiley.com/doi/pdf/10.1002/crat.201100125.

[26] Keller R, Geiss R. Transmission EBSD from 10 nm domains in a scanning electron microscope. J Microsc 2012;245(3):245–51. http://dx.doi.org/10.1111/j.1365-2818.2011.03566.x, URL: https://onlinelibrary.wiley.com/doi/abs/10.1111/j.1365-2818.2011.03566.x. _eprint: https://onlinelibrary.wiley.com/doi/pdf/10.1111/j.1365-2818.2011.03566.x.

[27] Trimby PW. Orientation mapping of nanostructured materials using transmission Kikuchi diffraction in the scanning electron microscope. Ultramicroscopy 2012;120:16–24. http://dx.doi.org/10.1016/j.ultramic.2012.06.004, URL: https://www.sciencedirect.com/science/article/pii/S0304399112001258.

[28] Brodusch N, Demers H, Gauvin R. Nanometres-resolution Kikuchi patterns from materials science specimens with transmission electron forward scatter diffraction in the scanning electron microscope. J Microsc 2013;250(1):1–14. http://dx.doi.org/10.1111/jmi.12007, URL: https://onlinelibrary.wiley.com/doi/abs/10.1111/jmi.12007. _eprint: https://onlinelibrary.wiley.com/doi/pdf/10.1111/jmi.12007.

[29] Viladot D, Véron M, Gemmi M, Peiró F, Portillo J, Estradé S, et al. Orientation and phase mapping in the transmission electron microscope using precession-assisted diffraction spot recognition: state-of-the-art results. J Microsc 2013;252(1):23–34. http://dx.doi.org/10.1111/jmi.12065, URL: https://onlinelibrary.wiley.com/doi/abs/10.1111/jmi.12065. _eprint: https://onlinelibrary.wiley.com/doi/pdf/10.1111/jmi.12065.

[30] Abbasi M, Kim D-I, Guim H-U, Hosseini M, Danesh-Manesh H, Abbasi M. Application of transmitted Kikuchi diffraction in studying nano-oxide and ultrafine metallic grains. ACS Nano 2015-11-24;9(11):10991–1002. http://dx.doi.org/10.1021/acsnano.5b04296, Publisher: American Chemical Society.

[31] Gao Q-Y, Li S-X, Su Y-S, Cao J, Moliar O. Grain coarsening of nano laminated structure in martensite steel under sliding wear. Tribol Int 2020;151:106381. http://dx.doi.org/10.1016/j.triboint.2020.106381, URL: https://www.sciencedirect.com/science/article/pii/S0301679X2030219X.

[32] Chi W, Wang W, Hou Z, Zhang M. Mechanism of mean stress sensitivity in Ti-6Al-4V under different stress ratios in high cycle fatigue. Int J Fatigue 2024-06-01;183:108268. http://dx.doi.org/10.1016/j.ijfatigue.2024.108268, URL: https://www.sciencedirect.com/science/article/pii/S0142112324001269.

[33] Sha G, Tugcu K, Liao XZ, Trimby PW, Murashkin MY, Valiev RZ, et al. Strength, grain refinement and solute nanostructures of an Al–Mg–Si alloy (AA6060) processed by high-pressure torsion. Acta Mater 2014-01-15;63:169–79. http://dx.doi.org/10.1016/j.actamat.2013.10.022, URL: https://www.sciencedirect.com/science/article/pii/S1359645413007738.

[34] Zhang H-J, Yu F, Li S-X, He E-G. Fine granular area formation by damage-induced shear strain localization in very-high-cycle fatigue. Fatigue Fract Eng Mater Struct 2021;44(9):2489–502. http://dx.doi.org/10.1111/ffe.13529, URL: https://onlinelibrary.wiley.com/doi/abs/10.1111/ffe.13529. _eprint: https://onlinelibrary.wiley.com/doi/pdf/10.1111/ffe.13529.

[35] Geathers J, Torbet C, Jones J, Daly S. Examining the role of water vapor on small fatigue crack growth behavior in Ti-6242S using ultrasonic fatigue and scanning electron microscopy. Int J Fatigue 2022;156:106672. http://dx.doi.org/10.1016/j.ijfatigue.2021.106672, URL: https://linkinghub.elsevier.com/retrieve/pii/S0142112321005144.

[36] Sinha V, Mills MJ, Williams JC. Determination of crystallographic orientation of dwell-fatigue fracture facets in Ti-6242 alloy. J Mater Sci 2007;42(19):8334–41. http://dx.doi.org/10.1007/s10853-006-0252-z, URL: http://link.springer.com/10.1007/s10853-006-0252-z.

[37] Themelis G, Chikwembani S, Weertman J. Determination of the orientation of Cu-Bi grain boundary facets using a photogrammetric technique. Mater Charact 1990;24(1):27–40. http://dx.doi.org/10.1016/1044-5803(90)90069-V, URL: https://linkinghub.elsevier.com/retrieve/pii/104458039090069V.

[38] Pilchak A, Bhattacharjee A, Rosenberger A, Williams J. Low ΔK faceted crack growth in titanium alloys. Int J Fatigue 2009;31(5):989–94. http://dx.doi.org/10.1016/j.ijfatigue.2008.03.036, URL: https://linkinghub.elsevier.com/retrieve/pii/S0142112308001035.

[39] Junet A. Étude tridimensionnelle de la propagation en fatigue de fissures internes dans les matériaux métalliques [Ph.D. thesis], France: Université de Lyon; 2021.

[40] Lavogiez C, Hémery S, Villechaise P. Concurrent operation of c + a slip and twinning under cyclic loading of Ti-6Al-4V. Scr Mater 2018;157:30–3. http://dx.doi.org/10.1016/j.scriptamat.2018.07.033, URL: https://linkinghub.elsevier.com/retrieve/pii/S1359646218304524.

[41] Jha SK, Szczepanski CJ, Golden PJ, Porter WJ, John R. Characterization of fatigue crack-initiation facets in relation to lifetime variability in Ti–6Al–4V. Int J Fatigue 2012;42:248–57. http://dx.doi.org/10.1016/j.ijfatigue.2011.11.017, URL: https://linkinghub.elsevier.com/retrieve/pii/S0142112311003148.

[42] Du L, Pan X, Hong Y. New insights into microstructure refinement in crack initiation region of very-high-cycle fatigue for SLM Ti-6Al-4V via precession electron diffraction. Materialia 2024-03-01;33:102008. http://dx.doi.org/10.1016/j.mtla.2024.102008, URL: https://www.sciencedirect.com/science/article/pii/S258915292400005X.

[43] Hong Y, Liu X, Lei Z, Sun C. The formation mechanism of characteristic region at crack initiation for very-high-cycle fatigue of high-strength steels. Int J Fatigue 2016;89:108–18. http://dx.doi.org/10.1016/j.ijfatigue.2015.11.029, URL: https://linkinghub.elsevier.com/retrieve/pii/S0142112315004296.

[44] Barr CM, Duong T, Bufford DC, Milne Z, Molkeri A, Heckman NM, et al. Autonomous healing of fatigue cracks via cold welding. Nature 2023;620(7974):552–6. http://dx.doi.org/10.1038/s41586-023-06223-0, URL: https://www.nature.com/articles/s41586-023-06223-0.

[45] Henaff G, Sarrazin-Baudoux C. Environmentally assisted fatigue in the gaseous atmosphere. Comprehensive structural integrity. Elsevier; 2023, p. 45–130. http://dx.doi.org/10.1016/B978-0-12-822944-6.00031-1, URL: https://linkinghub.elsevier.com/retrieve/pii/B9780128229446000311.

[46] Feng B, Chen JY, Qi SK, He L, Zhao JZ, Zhang XD. Characterization of surface oxide films on titanium and bioactivity. J Mater Sci, Mater Med 2002;13(5):457–64. http://dx.doi.org/10.1023/A:1014737831371.

[47] Oguma H. Formation mechanism of the distinctive granular fracture surface in subsurface fracture of Ti6Al4V alloy. Materialia 2022;21:101312. http://dx.doi.org/10.1016/j.mtla.2021.101312, URL: https://www.sciencedirect.com/science/article/pii/S2589152921003148.

[48] Williams JJ, Yazzie KE, Connor Phillips N, Chawla N, Xiao X, De Carlo F, et al. On the correlation between fatigue striation spacing and crack growth rate: A three-dimensional (3-D) X-ray synchrotron tomography study. Metall Mater Trans A 2011;42(13):3845–8. http://dx.doi.org/10.1007/s11661-011-0963-x, URL: http://link.springer.com/10.1007/s11661-011-0963-x.

[49] Chi W, Wang W, Wu L, Duan G, Sun C. Nanograin formation mechanism under fatigue loadings in additively manufactured Ti-6Al-4V alloy. Int J Fatigue 2023;175:107821. http://dx.doi.org/10.1016/j.ijfatigue.2023.107821, URL: https://linkinghub.elsevier.com/retrieve/pii/S0142112323003225.

[50] Rugg D, Dixon M, Dunne FPE. Effective structural unit size in titanium alloys. J Strain Anal Eng Des 2007;42(4):269–79. http://dx.doi.org/10.1243/03093247JSA273, URL: http://journals.sagepub.com/doi/10.1243/03093247JSA273.

[51] Ma Y, Xue Q, Wang H, Huang S, Qiu J, Feng X, et al. Deformation twinning in fatigue crack tip plastic zone of Ti-6Al-4V alloy with Widmanstatten microstructure. Mater Charact 2017;132:338–47. http://dx.doi.org/10.1016/j.matchar.2017.08.029, URL: https://linkinghub.elsevier.com/retrieve/pii/S1044580317316625.

[52] Sun C, Wu H, Chi W, Wang W, Zhang G-P. Nanograin formation and cracking mechanism in Ti alloys under very high cycle fatigue loading. Int J Fatigue 2023;167:107331. http://dx.doi.org/10.1016/j.ijfatigue.2022.107331, URL: https://linkinghub.elsevier.com/retrieve/pii/S0142112322005813.

[53] Munroe N, Tan X, Gu H. Orientation dependence of slip and twinning in HCP metals. Scr Mater 1997;36(12):1383–6. http://dx.doi.org/10.1016/S1359-6462(97)00048-1, URL: https://linkinghub.elsevier.com/retrieve/pii/S1359646297000481.

[54] Dancette S. pyOriMap - Analysis of large crystallographic orientation datasets in python. 2024, URL: https://github.com/sdancette/pyorimap. original-date: 2024-06-05T14:57:39Z.

[55] Bilby B, Crocker A. The theory of the crystallography of deformation twinning. Proc R Soc A 1965;288(1413):240–55. http://dx.doi.org/10.1098/rspa.1965.0216, URL: https://royalsocietypublishing.org/doi/10.1098/rspa.1965.0216.

[56] Dancette S, Delannay L, Renard K, Melchior M, Jacques P. Crystal plasticity modeling of texture development and hardening in TWIP steels. Acta Mater 2012;60(5):2135–45. http://dx.doi.org/10.1016/j.actamat.2012.01.015, URL: http://linkinghub.elsevier.com/retrieve/pii/S135964541200050X.

[57] Castioni F, Cazottes S, Rollett AD, Dancette S. Plastic behavior of the α' phase in Ti-6Al-4V alloys. Mater Lett 2021;283:128719. http://dx.doi.org/10.1016/j.matlet.2020.128719.

[58] Bridier F, McDowell DL, Villechaise P, Mendez J. Crystal plasticity modeling of slip activity in Ti–6Al–4V under high cycle fatigue loading. Int J Plast 2009;25(6):1066–82. http://dx.doi.org/10.1016/j.ijplas.2008.08.004, URL: https://linkinghub.elsevier.com/retrieve/pii/S0749641908001265.

[59] Lavogiez C, Dancette S, Cazottes S, Le Bourlot C, Maire E. In situ analysis of plasticity and damage nucleation in a Ti-6Al-4V alloy and laser weld. Mater Charact 2018;146:81–90. http://dx.doi.org/10.1016/j.matchar.2018.09.039, URL: https://www.sciencedirect.com/science/article/pii/S1044580318316127.

[60] Britton TB, Dunne FPE, Wilkinson AJ. On the mechanistic basis of deformation at the microscale in hexagonal close-packed metals. Proc. R. Soc. A 2015;471(2178):20140881. http://dx.doi.org/10.1098/rspa.2014.0881, URL: https://royalsocietypublishing.org/doi/10.1098/rspa.2014.0881.